

Direct observation of linear dispersion close to the Fermi level in the topological semimetal WTe_2 through Landau quantization at atomic scale

Raquel Sánchez-Barquilla,¹ Francisco Martín Vega,¹ Alberto M. Ruiz,² Na Hyun Jo*,³ Edwin Herrera,¹ José J. Baldoví,² Masayuki Ochi,^{4,5} Ryotaro Arita,⁶ Sergey L. Bud'ko,³ Paul C. Canfield,³ Isabel Guillamón,¹ and Hermann Suderow¹

¹*Laboratorio de Bajas Temperaturas y Altos Campos Magnéticos, Departamento de Física de la Materia Condensada, Instituto Nicolás Cabrera and Condensed matter Physics Center (IFIMAC), Unidad Asociada UAM-CSIC, Universidad Autónoma de Madrid, E-18049, Madrid, Spain*

²*Instituto de Ciencia Molecular (ICMol), Universidad de Valencia, Catedrático José Beltrán 2, 46980 Paterna, Spain*

³*Ames Laboratory and Department of Physics & Astronomy, Iowa State University, Ames, IA 50011**

⁴*Forefront Research Center, Osaka University, Toyonaka, Osaka 560-0043, Japan*

⁵*Department of Physics, Osaka University, Toyonaka, Osaka 560-0043, Japan*

⁶*RIKEN Center for Emergent Matter Science, Wako, Saitama 351-0198, Japan*

(Dated: May 24, 2024)

We study the topological Weyl type-II semimetal WTe_2 via Scanning Tunneling Microscopy (STM) and Density Functional Theory calculations (DFT). We successfully determine the band structure at zero field close to the Fermi level by comparing quasiparticle interference (QPI) experiments with DFT. Under magnetic fields, we observe Landau level quantization on atomic scale measurements and find a level sequence evidencing a linearly dispersing portion of the band structure. Our results establish the long sought connection between Weyl cones and Landau quantization in WTe_2 . Atomic scale Landau quantization emerges as a powerful probe of topological surface states for semimetals, superconductors and topological insulators.

Electrons under magnetic fields in a solid perform quantized motion at a plane perpendicular to the magnetic field. The bulk boundary correspondence leads to topologically protected surface states in materials presenting non trivial crossing in the band structure as Dirac or Weyl points [1–10]. Landau quantization of these surface bands can lead to chiral conduction channels [1–7, 11–13].

WTe_2 is a Van der Waals layered semimetal with conical tilted crossings leading to Weyl fermions [12, 14–29]. Slight distortions that preserve symmetry lead to a higher order topological insulator driven by double band inversion [30].

Landau quantization leads to pronounced features in WTe_2 in practically all probes under magnetic fields [15, 31, 32]. In few and single layers, anomalous magnetic transport properties as the quantum spin Hall effect possibly related to helical edge states have been observed [33–36]. The connection between Landau levels and the linearly dispersing band structure close to Weyl points or at surface Dirac points remains however difficult to establish.

Scanning Tunneling Microscopy (STM) seems adequate to study the band structure at zero field through quasiparticle interference (QPI) at impurities or defects. Landau levels, on the other hand, have been observed with STM only in a few compounds as graphene or

bismuth and in two-dimensional electron gases [37–45]. Both, extremely clean samples and well defined two-dimensional single or few band electronic properties are needed. The energy between two Landau levels ΔE is, due to the small effective masses in WTe_2 , in the meV range and thus accessible to STM. But the band structure of WTe_2 is quite intricate, with several overlapping electron and hole bands [12, 15, 16, 18–20, 23, 24]. Here we make detailed atomic scale STM experiments at zero and under magnetic fields on WTe_2 . We determine the band structure at zero field by comparing QPI and Density Functional Theory (DFT) calculations, and unveil Landau quantization under magnetic fields.

We performed STM measurements using a home-made STM described in Ref. [46] and the software described in Ref. [47]. For image and spectroscopy treatment we used the software described in Refs. [47, 48]. The samples were grown from a Te-rich binary melt, as described in Refs [19, 49]. The crystals are plate-like with typical dimensions of 2 mm \times 0.1 mm \times 0.01 mm, and the crystallographic c -axis perpendicular to the crystal surface. We exfoliated the sample in-situ in cryogenic conditions by gluing a post and pushing it at low temperatures using the in-situ slider described in Ref. [46]. This method allows to obtain large, clean and flat surfaces, showing atomic rows and interstitial sites, similar to those reported before [23, 24, 29, 50, 51]. We successfully cleaved eight crystals, in which we changed the field of view more than a hundred times. Experiments were made in a helium bath cryostat at 4.2K. Using an in-situ sample positioning system [46], we studied hundreds of fields of view, some with defects and impurities, where

* Present address: Department of Physics, University of Michigan, Ann Arbor, MI 48109, USA

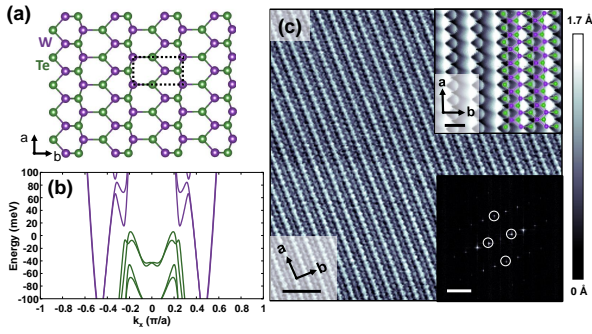


FIG. 1. (a) Atomic structure of the surface of WTe_2 . Dashed black rectangle is the unit cell. W atoms are shown in violet and Te atoms in green. The surface is composed of Te atoms, the W atoms lie at the next plane. (b) Band dispersion of WTe_2 calculated using Density Functional Theory (DFT). W-derived bands are shown in violet and Te-derived bands in green. Here we show only the dispersion along the a direction (k_x). The band structure along another direction is provided in the Supplementary Material (Fig. S2). (c) Topographic STM image of WTe_2 . Black horizontal scale bar is 2 nm long. In the upper right we show a zoom where we have superposed the atomic structure (horizontal black scale bar is 0.5 nm long). In the lower right panel we show the Fourier transform, with the main crystal Bragg peaks surrounded by white circles (white horizontal scale bar is 3 nm^{-1} long). Black arrows provide the in-plane lattice directions.

we took the QPI data, and others completely free of impurities, where we observed Landau quantization.

We performed first-principles band structure calculations based on DFT with the generalized gradient approximation with the Perdew-Burke-Ernzerhof parametrization [52] and the full-potential (linearized) augmented plane-wave plus local orbitals method including the spin-orbit coupling as implemented in the WIEN2K code [53, 54]. We took the experimental crystal structure from Ref. [55]. The maximum modulus for the reciprocal lattice vectors K_{max} was chosen so that $rK_{\text{max}} = 8$, where the muffin-tin radius r was 2.5 Bohr for both W and Te atoms.

The surface atomic structure is defined by the Van der Waals gap and consists of layers where the topmost atomic lattice is formed by arrangements of Te atoms. In our STM images, we identify the Te atomic positions and the underlying W atoms in between (see Fig. 1(a,c)). The surface presents a very small number of defects, consisting mostly on W-Te substitutions and vacancies. As shown in the Supplementary Material (Fig. S1) there is approximately one defect per 700 atoms, which gives 10^{12} defects per cm^{-2} , a value that is compatible with the extremely high residual resistance ratio reported in the same crystals and the neat observation of quantum oscillations in macroscopic experiments [18, 19, 56].

These defects are scattering centers and provide the oscillatory pattern in the density of states that we can image through QPI. The result of our QPI measurements is shown in Fig. 2(a). We compare the Fourier transform of

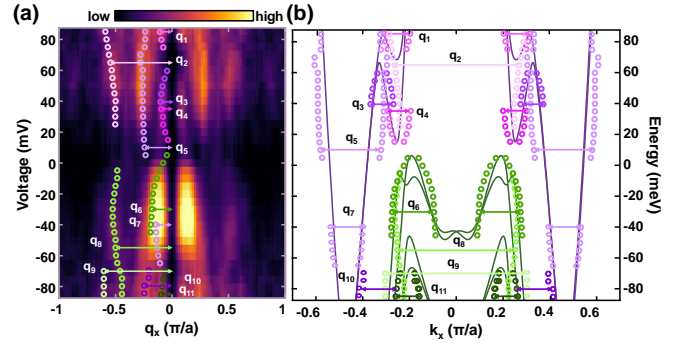


FIG. 2. (a) Color map showing the scattering intensity (color scale following the bar on the top) as a function of the bias voltage and the scattering along q_x . q_x corresponds to the a direction in real space. More data and details are provided in the Supplementary Material. Colored dots trace the different scattering vectors in the bias voltage- q_x plane. (b) The band structure calculated by DFT is shown as colored lines as a function of the energy and the wavevector k_x . Violet and green are for W- and Te-derived bands respectively. The scattering vectors shown in (a) are represented in (b) as pairs of colored dots using the same color code. Arrows represent some of the main scattering vectors, also marked as \mathbf{q}_1 to \mathbf{q}_{11} .

the scattering pattern with the band structure obtained from DFT calculations in Fig. 2(b). The scattering vectors along q_x join portions of the band structure located at k_x and $k_y = 0$. For example, intraband scattering joining states at $\pm k_x$ gives $q = 2k_x$ (as the light violet arrow \mathbf{q}_2 on top of Fig. 2(a,b)). Intraband scattering joining states at either side of a pocket provides $q = \delta k_x$ where δk_x is the pocket size (as the dark green arrows \mathbf{q}_6 in the lower middle of Fig. 2(a,b)). More details are provided in the Supplementary Material, Fig. S2. We observe scattering patterns, elongated along the a -direction (x in Fig. 2(a,b)), which is the direction of the Te chains (Fig. 1(b), see Supplementary Material, Fig. S2, for results out of the a direction).

Starting at large and positive bias voltages we find a large scattering vector (light violet arrow, \mathbf{q}_2 in Fig. 2(a)) due to intraband scattering between the outer sides of the small electron pockets shown in Fig. 2(b). This vector decreases in size when decreasing the energy, and disappears close to 20 meV, where we also find the bottom of the small electron band (Fig. 2(b)). We find a few smaller scattering vectors (dark violet and magenta arrows, $\mathbf{q}_{1,3,4}$ in Fig. 2(a,b)) associated with the intra-band scattering within electron pockets located at large k_x , and with a small hole like portion of the band structure. A large vector due to intra-band scattering within the electron pockets at large k_x decreases in size when decreasing the voltage (light violet arrow, \mathbf{q}_5 , in Fig. 2(a,b)), and the corresponding features mix with other scattering vectors. At small negative bias voltages we find scattering from the same band again (light violet arrow, \mathbf{q}_7 , in Fig. 2(a,b)), with a considerably reduced size. We also find a small interband scattering vector

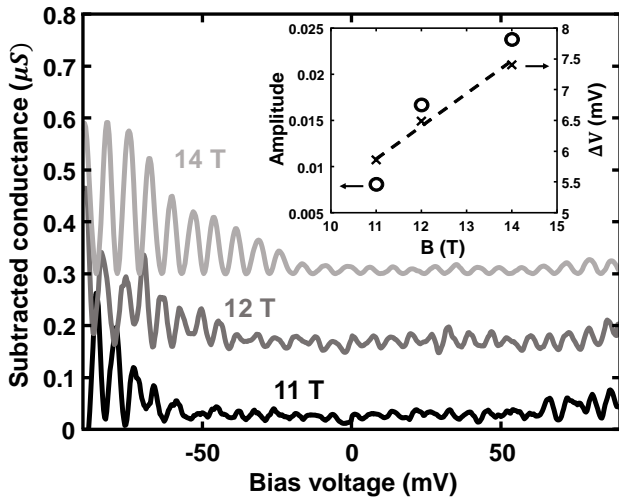


FIG. 3. Conductance vs bias voltage at 11 T, 12 T and 14 T. A background has been removed and curves shifted for clarity. In the inset we show the amplitude of the oscillatory component as circles and the separation between peaks as crosses. The dashed line provides the Landau quantization expected for a mass of $m^* = 0.22m_e$.

between electron and hole bands (bright violet \mathbf{q}_{10} in Fig. 2(a)). For the Te derived bands we find a vector due to intra-band scattering of two hole bands (green arrow \mathbf{q}_6 in Fig. 2(a,b)) and large scattering vectors associated to intraband scattering in a hole like band at smaller energies (green arrow $\mathbf{q}_{8,9}$ in Fig. 2(a,b)). The band structure below the Fermi level is mostly compatible with angular resolved photoemission experiments probing filled states [18, 19, 51]. Thus, in all, our QPI measurements provide a rather complete view of the band structure of WTe₂ around the Fermi level.

A detailed comparison between theory and experiment (Supplemental Material, Fig. S3) shows evidence for surface states at the energy positions predicted by calculations. Nevertheless, it is difficult to distinguish these surface states from bulk features in the scattering pattern. As we shall see below, Landau quantization provides further insight.

The presence of defects is in principle detrimental to observe Landau quantization [58]. A relevant scale for obtaining Landau levels is the magnetic length $\ell_B = \sqrt{\hbar/eB}$, which is related with the radius of the cyclotron orbit $r_n = \sqrt{2n+1}\ell_B$. To resolve the Landau levels in the density of states, the distance between the defects must be of the order or larger than ℓ_B . At 14 T, the Landau orbits are of the order of $r_0 \approx \ell_B \approx 7$ nm, which is much lower than the mean free path ℓ , so that, in principle, one can expect the observation of Landau levels in the tunneling conductance under a magnetic field. However, the tunneling conductance obtained by spatially averaging results over large fields, even when these are completely free of impurities (Supplemental Material, Fig. S4), presents no significant changes as a function of

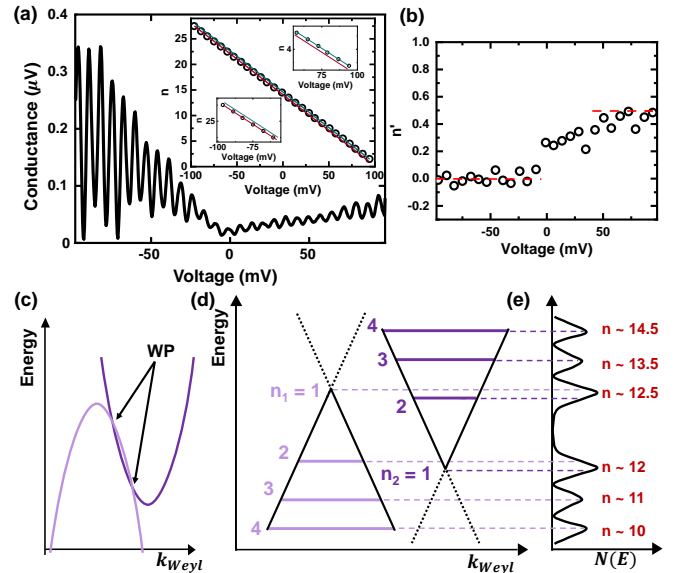


FIG. 4. (a) Tunneling conductance vs bias voltage obtained at 14 T. In the inset we plot the index of the Landau level n as a function of the voltage. n is arbitrarily set to zero at the start of the curve for large positive bias voltages. The blue line is obtained when fitting the Landau level index to a straight line for positive bias voltages, and the red line is obtained when fitting data for negative bias voltages. (b) We plot as circles the difference between the red line and the observed Landau level index, obtained from the inset in (a). Red dashed line shows the result using two linearly dispersing Dirac cones. (c) Schematic representation of two perfectly compensated electron (violet) and hole (light violet) bands that cross at two Weyl points (marked by the arrow). Weyl points arise in WTe₂ on crossing linearly dispersing bands above the Fermi level and at a certain angle to a crystalline direction, marked in the figure by k_{Weyl} [12]. The dispersion relation is linear at Weyl points [57]. (d) Schematic representation of a projection of linear dispersing bands, as occurring on two Weyl points located close in energy. For clarity, we only show one half of the cone around each Weyl point. Landau level quantization for a magnetic field applied along the c-axis is schematically shown as horizontal colored lines. Level separation is given by the linear dispersion relation. (e) As a black line, we show the k-integrated density of states as a function of the energy, considering smeared Landau levels and the overlap between bands. The sequence of Landau levels, when counting from low to high energies, is maximally shifted (by 1/2) in the energy range where electron and hole bands overlap.

the magnetic field. This absence of Landau levels in the tunneling conductance cannot be due to impurity scattering. Instead, it must be related to the intricate band structure with multiple bands.

To address this issue, we note that tunneling with STM occurs through the overlap between sample and tip wavefunctions [59]. The tunneling overlap on different atomic sites is different, involving different portions of the band structure [60–63]. As we show in Fig. 1(c), we observe Te atomic rows and distinct contrast in between Te sites. Thus, we can expect tunneling dominated by Te derived

bands on the Te sites and by W derived bands in between. If we take tunneling conductance curves at a single atomically defined location, we observe strong oscillations of the tunneling conductance as a function of the bias voltage (Fig. 3). The amplitude of the oscillations increases with magnetic field. From the Fourier Transform of the tunneling conductance vs bias voltage curves, we obtain a single peak that corresponds to $\Delta E \propto \hbar\omega_c$, the separation in energy between the levels. Using $\omega_c = \frac{eB}{m^*}$ we obtain an effective mass $m^* = 0.22m_e$ (inset of Fig. 3). The effective mass obtained is similar to the values reported before and compatible with the band dispersion observed through QPI described above. Notice that all the bands crossing the Fermi level have very similar effective masses, so the separation between the levels is not expected to change significantly for the different bands. For example, a difference of $0.04m_e$ results in a difference in energy of only 1.2 meV. This, and other broadening effects, discussed in the Supplemental Material, influence the shape of the peaks, which are about 5 mV wide. Furthermore, the phase of the oscillation changes with the atomic position, leading to characteristic patterns that can be reproduced using a shift in the Landau level sequence due to different band selectivity at each atomic site (see Supplemental Material, Fig. S5). Thus, it is possible to observe Landau levels in the tunneling conductance of a material with a three dimensional dispersion and multiple bands, provided that there are no large differences in the effective mass between different bands and the atomic scale tunneling selectivity is sufficiently well developed.

To gain further insight we plot in Fig. 4(a) the atomically resolved tunneling conductance vs bias voltage obtained at 14 T, where the signal is largest. When numbering the levels and plotting the resulting quantum numbers n as a function of the bias voltage, we observe at first sight a straight line. But a closer look shows that, although the slope of n vs the bias voltage is the same for all bias voltages, there is a shift at positive bias. To better see this shift, we fit the n vs bias voltage to a straight line for large positive and negative bias voltages, and show the subtraction in Fig. 4(b), where we observe a shift by $1/2$. To explain this we recall Landau quantization around Weyl crossings as schematically shown in Fig. 4(c-e). Weyl semimetals are characterized by a band crossing producing at least two points with linear dispersion close to the Fermi level (Fig. 4(c)). The level quantization along the linearly dispersing band structure follows a $\sqrt{|E - E_0|}$ dependence, where E_0 is the crossing point. A density of states measurement includes contributions from both bands and leads to a mixed Landau level sequence (Fig. 4(e)). As discussed above, due to three dimensional band dispersion, lifted band degeneracy or the influence of impurities, the Landau levels broaden. As a consequence, the lowest Landau levels of each band appear as a single peak in the density of states (Fig. 4(e)). However, when counting the Landau level index n on a given energy window, we observe a shift of

$1/2$ within the energy window where both bands overlap (Fig. 4(b,e)). This shift does not occur when dispersion relations are quadratic, because it is caused by the enhanced level separation close to E_0 from the $\sqrt{|E - E_0|}$ dependence. Thus, our data show that there are linear crossings within the studied energy window.

It was shown that Landau quantization in type-II Weyl semimetals depends on the angle between the direction of the line joining the Weyl nodes and the magnetic field [64–66]. There is an angle for which the Landau levels collapse due to the distortion of circular orbits induced by the Weyl tilt [12, 64–69]. This suggests that the amplitude of Landau levels and the sequence we observe here should change considerably with the direction of the magnetic field. There are 16 predicted Weyl points, most at finite k_x and k_y and some at finite k_z [12]. To the best of our knowledge, there is yet no available STM operating on a rotating field above 10 T. If this is achieved, studying the angular dependent of Landau levels in WTe₂ could be used to trace the multiplicity of Weyl nodes.

The consequence of Weyl crossings at the surface of bulk WTe₂ could become visible in studies of heterostructures. Thanks to the layered structure of transition metal dichalcogenides, heterostructures of WTe₂ with layered superconductors and magnets have been fabricated [70–72]. These provide in-gap states in proximity induced superconductivity, non-reciprocal Josephson currents, a Josephson current comparable to a single chiral conduction channel at hinge states, or the possibility to tune the magnetization of a magnetic layer on top of WTe₂ [70–74]. Our observation of Landau quantized states and Weyl cones suggests the presence of chiral edge modes at the surface. This is strongly supported by the observation of increased amplitude Landau oscillations in the energy range where surface states are expected (see Supplemental Material, Fig. S6). The chiral edge modes have topologically protected chiral currents moving in opposite directions when the magnetic field and the current is applied perpendicular to the planes. It would be interesting to address transport studies in heterostructures based on WTe₂ with the new perspective opened by our data.

It is noteworthy that WTe₂ presents ferroelectric properties, being one of the few polar metals known so far [75–77]. In few and single layers of WTe₂ a gap is observed under magnetic fields [35]. The origin of this gap opening is under debate. A charge density wave and a Coulomb gap have been considered as possibilities [34, 78]. Both should be characteristic distortions of the band structure in the single or few layer limit. Our results confirm that this system, being very sensitive to distortions, has a linearly dispersing band structure in the semimetallic phase.

In summary, we have determined the band structure close to the Fermi level in WTe₂ using QPI, obtaining an excellent agreement with DFT calculations. We demonstrate the existence of linear dispersion in WTe₂ due to Weyl nodes at crossing points of electron and hole

bands. Our data show that Landau level quantization can be observed at the surface of materials with a three-dimensional dispersion relation, provided that there is well differentiated tunneling on different atomic positions. This opens interesting prospects, which might help understanding magnetic field properties of materials having unconventional surface states as PtSn_4 or NdBi , or potentially strong dependencies of the band structure with the magnetic field, as UTe_2 [8, 9, 79–82].

Acknowledgments. This work was supported by the Spanish Research State Agency (PID2020-114071RB-I00, CEX2023001316-M, TED2021-130546B-I00, PDC2021-121086-I00), by the Comunidad de Madrid through program NANOMAGCOST-CM (Program No.S2018/NMT-4321), by the European Research

Council PNICTEYES grant agreement 679080, and by VectorFieldImaging grant agreement 101069239. We acknowledge collaborations through EU program Cost CA21144 (Superqumap). We acknowledge segainvex for design and construction of STM and cryogenic equipment. Work at Valencia received support from the European Union (ERC-2021-StG-101042680 2D-SMARTiES) and the Gen-T programme of the Generalitat Valenciana (CIDEXG/2023/1). A.M.R. thanks the Spanish MIU (FPU21/04195). Work at the Ames National Laboratory was supported by the U.S. Department of Energy, Office of Science, Basic Energy Sciences, Materials Sciences and Engineering Division. Ames National Laboratory is operated for the U.S. Department of Energy by Iowa State University under Contract No. DE-AC02-07CH11358.

-
- [1] M. Z. Hasan and C. L. Kane, Colloquium: Topological insulators, *Rev. Mod. Phys.* **82**, 3045 (2010).
- [2] X.-L. Qi and S.-C. Zhang, Topological insulators and superconductors, *Rev. Mod. Phys.* **83**, 1057 (2011).
- [3] B. J. Wieder, B. Bradlyn, J. Cano, Z. Wang, M. G. Vergniory, L. Elcoro, A. A. Soluyanov, C. Felser, T. Neupert, N. Regnault, and B. A. Bernevig, Topological materials discovery from crystal symmetry, *Nature Reviews Materials* **7**, 196 (2022).
- [4] N. Nagaosa, T. Morimoto, and Y. Tokura, Transport, magnetic and optical properties of weyl materials, *Nature Reviews Materials* **5**, 621 (2020).
- [5] B. Yan and C. Felser, Topological materials: Weyl semimetals, *Annual Review of Condensed Matter Physics* **8**, 337 (2017).
- [6] N. P. Armitage, E. J. Mele, and A. Vishwanath, Weyl and dirac semimetals in three-dimensional solids, *Rev. Mod. Phys.* **90**, 015001 (2018).
- [7] B. Q. Lv, T. Qian, and H. Ding, Experimental perspective on three-dimensional topological semimetals, *Rev. Mod. Phys.* **93**, 025002 (2021).
- [8] E. Mun, H. Ko, G. J. Miller, G. D. Samolyuk, S. L. Bud'ko, and P. C. Canfield, Magnetic field effects on transport properties of PtSn_4 , *Phys. Rev. B* **85**, 035135 (2012).
- [9] Y. Wu, L.-L. Wang, E. Mun, D. D. Johnson, D. Mou, L. Huang, Y. Lee, S. L. Bud'ko, P. C. Canfield, and A. Kaminski, Dirac node arcs in PtSn_4 , *Nature Physics* **12**, 667 (2016).
- [10] H. Inoue, A. Gyenis, Z. Wang, J. Li, S. W. Oh, S. Jiang, N. Ni, B. A. Bernevig, and A. Yazdani, Quasiparticle interference of the Fermi arcs and surface-bulk connectivity of a Weyl semimetal, *Science* **351**, 1184 (2016).
- [11] T. Yu, Z. Luo, and G. E. Bauer, Chirality as generalized spin-orbit interaction in spintronics, *Physics Reports* **1009**, 1 (2023), chirality as Generalized Spin-Orbit Interaction in Spintronics.
- [12] A. A. Soluyanov, D. Gresch, Z. Wang, Q. Wu, M. Troyer, X. Dai, and B. A. Bernevig, Type-II Weyl semimetals, *Nature* **527**, 495 (2015).
- [13] P. J. W. Moll, N. L. Nair, T. Helm, A. C. Potter, I. Kimchi, A. Vishwanath, and J. G. Analytis, Transport evidence for fermi-arc-mediated chirality transfer in the Dirac semimetal Cd_3As_2 , *Nature* **535**, 266 (2016).
- [14] H. Weyl, Elektron und gravitation. I, *Zeitschrift für Physik* **56**, 330 (1929).
- [15] M. N. Ali, J. Xiong, S. Flynn, J. Tao, Q. D. Gibson, L. M. Schoop, T. Liang, N. Haldolaarachchige, M. Hirschberger, N. P. Ong, and R. J. Cava, Large, non-saturating magnetoresistance in WTe_2 , *Nature* **514**, 205 (2014).
- [16] P. K. Das, D. D. Sante, F. Cilento, C. Bigi, D. Kopic, D. Soranzio, A. Sterzi, J. A. Krieger, I. Vobornik, J. Fujii, T. Okuda, V. N. Strocov, M. B. H. Breese, F. Parmigiani, G. Rossi, S. Picozzi, R. Thomale, G. Sangiovanni, R. J. Cava, and G. Panaccione, Electronic properties of candidate type-II Weyl semimetal WTe_2 : a review perspective, *Electronic Structure* **1**, 014003 (2019).
- [17] S. Xu, I. Belopolski, N. Alidoust, M. Neupane, G. Bian, C. Zhang, R. Sankar, G. Chang, Z. Yuan, C. Lee, S. Huang, H. Zheng, J. Ma, D. S. Sanchez, B. Wang, A. Bansil, F. Chou, P. P. Shibayev, H. Lin, S. Jia, and M. Z. Hasan, Discovery of a Weyl fermion semimetal and topological Fermi arcs, *Science* **349**, 613 (2015).
- [18] Y. Wu, D. Mou, N. H. Jo, K. Sun, L. Huang, S. L. Bud'ko, P. C. Canfield, and A. Kaminski, Observation of Fermi arcs in the type-II Weyl semimetal candidate WTe_2 , *Phys. Rev. B* **94**, 121113 (2016).
- [19] Y. Wu, N. H. Jo, M. Ochi, L. Huang, D. Mou, S. L. Bud'ko, P. C. Canfield, N. Trivedi, R. Arita, and A. Kaminski, Temperature-induced lifshitz transition in WTe_2 , *Phys. Rev. Lett.* **115**, 166602 (2015).
- [20] C. Wang, Y. Zhang, J. Huang, S. Nie, G. Liu, A. Liang, Y. Zhang, B. Shen, J. Liu, C. Hu, Y. Ding, D. Liu, Y. Hu, S. He, L. Zhao, L. Yu, J. Hu, J. Wei, Z. Mao, Y. Shi, X. Jia, F. Zhang, S. Zhang, F. Yang, Z. Wang, Q. Peng, H. Weng, X. Dai, Z. Fang, Z. Xu, C. Chen, and X. J. Zhou, Observation of Fermi arc and its connection with bulk states in the candidate type-II Weyl semimetal WTe_2 , *Phys. Rev. B* **94**, 241119 (2016).
- [21] J. Sánchez-Barriga, M. G. Vergniory, D. Evtushinsky, I. Aguilera, A. Varykhalov, S. Blügel, and O. Rader, Surface Fermi arc connectivity in the type-II Weyl semimetal candidate WTe_2 , *Phys. Rev. B* **94**, 161401 (2016).

- [22] F. Y. Bruno, A. Tamai, Q. S. Wu, I. Cucchi, C. Barreteau, A. de la Torre, S. McKeown Walker, S. Riccò, Z. Wang, T. K. Kim, M. Hoesch, M. Shi, N. C. Plumb, E. Giannini, A. A. Soluyanov, and F. Baumberger, Observation of large topologically trivial Fermi arcs in the candidate type-II Weyl semimetal WTe_2 , *Phys. Rev. B* **94**, 121112 (2016).
- [23] W. Zhang, Q. Wu, L. Zhang, S.-W. Cheong, A. A. Soluyanov, and W. Wu, Quasiparticle interference of surface states in the type-II Weyl semimetal WTe_2 , *Phys. Rev. B* **96**, 165125 (2017).
- [24] Y. Yuan, X. Yang, L. Peng, Z.-J. Wang, J. Li, C.-J. Yi, J.-J. Xian, Y.-G. Shi, and Y.-S. Fu, Quasiparticle interference of Fermi arc states in the type-II Weyl semimetal candidate WTe_2 , *Phys. Rev. B* **97**, 165435 (2018).
- [25] X.-C. Pan, X. Chen, H. Liu, Y. Feng, Z. Wei, Y. Zhou, Z. Chi, L. Pi, F. Yen, F. Song, X. Wan, Z. Yang, B. Wang, G. Wang, and Y. Zhang, Pressure-driven dome-shaped superconductivity and electronic structural evolution in tungsten ditelluride, *Nature Communications* **6**, 7805 (2015).
- [26] D. Kang, Y. Zhou, W. Yi, C. Yang, J. Guo, Y. Shi, S. Zhang, Z. Wang, C. Zhang, S. Jiang, A. Li, K. Yang, Q. Wu, G. Zhang, L. Sun, and Z. Zhao, Superconductivity emerging from a suppressed large magnetoresistant state in tungsten ditelluride, *Nature Communications* **6**, 7804 (2015).
- [27] G. Marini and M. Calandra, Light-tunable charge density wave orders in MoTe_2 and WTe_2 single layers, *Phys. Rev. Lett.* **127**, 257401 (2021).
- [28] E. Sajadi, T. Palomaki, Z. Fei, W. Zhao, P. Bement, C. Olsen, S. Luescher, X. Xu, J. A. Folk, and D. H. Cobden, Gate-induced superconductivity in a monolayer topological insulator, *Science* **362**, 922 (2018).
- [29] Y. Maximenko, Y. Chang, G. Chen, M. R. Hirsbrunner, W. Swiech, T. L. Hughes, L. K. Wagner, and V. Madhavan, Nanoscale studies of electric field effects on monolayer $1\text{T}'\text{-WTe}_2$, *npj Quantum Materials* **7**, 29 (2022).
- [30] Z. Wang, B. J. Wieder, J. Li, B. Yan, and B. A. Bernevig, Higher-order topology, monopole nodal lines, and the origin of large Fermi arcs in transition metal dichalcogenides $x\text{Te}_2$ ($x = \text{Mo}, \text{W}$), *Phys. Rev. Lett.* **123**, 186401 (2019).
- [31] P. S. Alekseev, A. P. Dmitriev, I. V. Gornyi, V. Y. Kachorovskii, B. N. Narozhny, M. Schütt, and M. Titov, Magnetoresistance in two-component systems, *Phys. Rev. Lett.* **114**, 156601 (2015).
- [32] Z. Zhu, X. Lin, J. Liu, B. Fauqué, Q. Tao, C. Yang, Y. Shi, and K. Behnia, Quantum Oscillations, Thermoelectric Coefficients, and the Fermi Surface of Semimetallic WTe_2 , *Phys. Rev. Lett.* **114**, 176601 (2015).
- [33] Z. Fei, T. Palomaki, S. Wu, W. Zhao, X. Cai, B. Sun, P. Nguyen, J. Finney, X. Xu, and D. H. Cobden, Edge conduction in monolayer WTe_2 , *Nature Physics* **13**, 677 (2017).
- [34] Z.-Y. Jia, Y.-H. Song, X.-B. Li, K. Ran, P. Lu, H.-J. Zheng, X.-Y. Zhu, Z.-Q. Shi, J. Sun, J. Wen, D. Xing, and S.-C. Li, Direct visualization of a two-dimensional topological insulator in the single-layer $1\text{T}' - \text{WTe}_2$, *Phys. Rev. B* **96**, 041108 (2017).
- [35] S. Wu, V. Fatemi, Q. D. Gibson, K. Watanabe, T. Taniguchi, R. J. Cava, and P. Jarillo-Herrero, Observation of the quantum spin Hall effect up to 100 Kelvin in a monolayer crystal, *Science* **359**, 76 (2018).
- [36] S. Tang, C. Zhang, D. Wong, Z. Pedramrazi, H.-Z. Tsai, C. Jia, B. Moritz, M. Claassen, H. Ryu, S. Kahn, J. Jiang, H. Yan, M. Hashimoto, D. Lu, R. G. Moore, C.-C. Hwang, C. Hwang, Z. Hussain, Y. Chen, M. M. Ugeda, Z. Liu, X. Xie, T. P. Devereaux, M. F. Crommie, S.-K. Mo, and Z.-X. Shen, Quantum spin Hall state in monolayer $1\text{T}'\text{-WTe}_2$, *Nature Physics* **13**, 683 (2017).
- [37] D. L. Miller, K. D. Kubista, G. M. Rutter, M. Ruan, W. A. de Heer, P. N. First, and J. A. Stroscio, Observing the quantization of zero mass carriers in graphene, *Science* **324**, 924 (2009).
- [38] J.-X. Yin, W. Ma, T. A. Cochran, X. Xu, S. S. Zhang, H.-J. Tien, N. Shumiya, G. Cheng, K. Jiang, B. Lian, Z. Song, G. Chang, I. Belopolski, D. Multer, M. Litskevich, Z.-J. Cheng, X. P. Yang, B. Swidler, H. Zhou, H. Lin, T. Neupert, Z. Wang, N. Yao, T.-R. Chang, S. Jia, and M. Zahid Hasan, Quantum-limit Chern topological magnetism in TbMn_6Sn_6 , *Nature* **583**, 533 (2020).
- [39] M. S. Hossain, F. Schindler, R. Islam, Z. Muhammad, Y.-X. Jiang, Z.-J. Cheng, Q. Zhang, T. Hou, H. Chen, M. Litskevich, B. Casas, J.-X. Yin, T. A. Cochran, M. Yahyavi, X. P. Yang, L. Balicas, G. Chang, W. Zhao, T. Neupert, and M. Z. Hasan, A hybrid topological quantum state in an elemental solid, *Nature* (2024).
- [40] B. E. Feldman, M. T. Randeria, A. Gyenis, F. Wu, H. Ji, R. J. Cava, A. H. MacDonald, and A. Yazdani, Observation of a nematic quantum hall liquid on the surface of bismuth, *Science* **354**, 316 (2016).
- [41] T. Hanaguri, K. Igarashi, M. Kawamura, H. Takagi, and T. Sasagawa, Momentum-resolved Landau-level spectroscopy of Dirac surface state in Bi_2Se_3 , *Phys. Rev. B* **82**, 081305 (2010).
- [42] Y. Okada, M. Serbyn, H. Lin, D. Walkup, W. Zhou, C. Dhital, M. Neupane, S. Xu, Y. J. Wang, R. Sankar, F. Chou, A. Bansil, M. Z. Hasan, S. D. Wilson, L. Fu, and V. Madhavan, Observation of Dirac node formation and mass acquisition in a topological crystalline insulator, *Science* **341**, 1496 (2013).
- [43] T. Johnsen, C. Schattauer, S. Samaddar, A. Weston, M. J. Hamer, K. Watanabe, T. Taniguchi, R. Gorbachev, F. Libisch, and M. Morgenstern, Mapping quantum Hall edge states in graphene by scanning tunneling microscopy, *Phys. Rev. B* **107**, 115426 (2023).
- [44] J. R. Bindel, J. Ulrich, M. Liebmann, and M. Morgenstern, Probing the nodal structure of Landau level wave functions in real space, *Phys. Rev. Lett.* **118**, 016803 (2017).
- [45] Y.-C. Tsui, M. He, Y. Hu, E. Lake, T. Wang, K. Watanabe, T. Taniguchi, M. P. Zaletel, and A. Yazdani, Direct observation of a magnetic-field-induced Wigner crystal, *Nature* **628**, 287 (2024).
- [46] H. Suderow, I. Guillaumon, and S. Vieira, Compact very low temperature scanning tunneling microscope with mechanically driven horizontal linear positioning stage, *Review of Scientific Instruments* **82**, 033711 (2011).
- [47] F. Martín-Vega, V. Barrena, R. Sánchez-Barquilla, M. Fernández-Lomana, J. Benito Llorens, B. Wu, A. Fente, D. Perconte Duplain, I. Horcas, R. López, J. Blanco, J. A. Higuera, S. Mañas-Valero, N. H. Jo, J. Schmidt, P. C. Canfield, G. Rubio-Bollinger, J. G. Rodrigo, E. Herrera, I. Guillaumon, and H. Suderow, Simplified feedback control system for scanning tunneling microscopy, *Review of Scientific Instruments* **92**, 103705 (2021).

- [48] I. Horcas, R. Fernández, J. M. Gómez-Rodríguez, J. Colchero, J. Gómez-Herrero, and A. M. Baro, WSXM: A software for scanning probe microscopy and a tool for nanotechnology, *Review of Scientific Instruments* **78**, 013705 (2007).
- [49] P. C. Canfield and Z. Fisk, Growth of single crystals from metallic fluxes, *Philosophical Magazine B* **65**, 1117 (1992).
- [50] P. K. Das, D. Di Sante, I. Vobornik, J. Fujii, T. Okuda, E. Bruyer, A. Gyenis, B. E. Feldman, J. Tao, R. Ciancio, G. Rossi, M. N. Ali, S. Picozzi, A. Yazdani, G. Panaccione, and R. J. Cava, Layer-dependent quantum cooperation of electron and hole states in the anomalous semimetal WTe₂, *Nature Communications* **7**, 10847 (2016).
- [51] I. Pletikosić, M. N. Ali, A. V. Fedorov, R. J. Cava, and T. Valla, Electronic structure basis for the extraordinary magnetoresistance in WTe₂, *Phys. Rev. Lett.* **113**, 216601 (2014).
- [52] J. P. Perdew, K. Burke, and M. Ernzerhof, Generalized gradient approximation made simple, *Phys. Rev. Lett.* **77**, 3865 (1996).
- [53] P. Blaha, K. Schwarz, G. K. H. Madsen, D. Kvasnicka, J. Luitz, R. Laskowski, F. Tran, and M. L. D., *WIEN2k, An Augmented Plane Wave + Local Orbitals Program for Calculating Crystal Properties (Karlheinz Schwarz, Vienna University of Technology, Austria)* (2018).
- [54] P. Blaha, K. Schwarz, F. Tran, R. Laskowski, G. K. H. Madsen, and L. D. Marks, WIEN2k: An APW+lo program for calculating the properties of solids, *The Journal of Chemical Physics* **152**, 074101 (2020).
- [55] A. Mar, S. Jobic, and J. A. Ibers, *J. Am. Chem. Soc.* **114**, 8963 (1992).
- [56] N. H. Jo, L.-L. Wang, P. P. Orth, S. L. Bud'ko, and P. C. Canfield, Magnetoelastoresistance in WTe₂: Exploring electronic structure and extremely large magnetoresistance under strain, *Proceedings of the National Academy of Sciences* **116**, 25524 (2019).
- [57] L. Lu, Z. Wang, D. Ye, L. Ran, L. Fu, J. D. Joannopoulos, and M. Soljačić, Experimental observation of Weyl points, *Science* **349**, 622 (2015).
- [58] P. Cheng, C. Song, T. Zhang, Y. Zhang, Y. Wang, J. Jia, J. Wang, Y. Wang, B. Zhu, X. Chen, X. Ma, K. He, L. Wang, X. Dai, Z. Fang, X. Xie, X. Qi, C. Liu, S. Zhang, and Q. Xue, Landau quantization of topological surface states in Bi₂Se₃, *Phys. Rev. Lett.* **105**, 076801 (2010).
- [59] J. Tersoff and D. R. Hamann, Theory of the scanning tunneling microscope, *Phys. Rev. B* **31**, 805 (1985).
- [60] K. Cho, A. Fente, S. Teknowijoyo, M. A. Tanatar, K. R. Joshi, N. M. Nusran, T. Kong, W. R. Meier, U. Kaluarachchi, I. Guillamón, H. Suderow, S. L. Bud'ko, P. C. Canfield, and R. Prozorov, Nodeless multiband superconductivity in stoichiometric single-crystalline CaFe₄As₄, *Phys. Rev. B* **95**, 100502 (2017).
- [61] I. Guillamon, H. Suderow, F. Guinea, and S. Vieira, Intrinsic atomic-scale modulations of the superconducting gap of 2h-nbse₂, *Phys. Rev. B* **77**, 134505 (2008).
- [62] F. Calleja, A. Arnau, J. J. Hinarejos, A. L. Vázquez de Parga, W. A. Hofer, P. M. Echenique, and R. Miranda, Contrast reversal and shape changes of atomic adsorbates measured with scanning tunneling microscopy, *Phys. Rev. Lett.* **92**, 206101 (2004).
- [63] H. Kim, Y. Yoshida, C.-C. Lee, T.-R. Chang, H.-T. Jeng, H. Lin, Y. Haga, Z. Fisk, and Y. Hasegawa, Atomic-scale visualization of surface-assisted orbital order, *Science Advances* **3**, eaao0362 (2017).
- [64] Z.-M. Yu, Y. Yao, and S. A. Yang, Predicted unusual magnetoresistance in type-II Weyl semimetals, *Phys. Rev. Lett.* **117**, 077202 (2016).
- [65] S. Tchoumakov, M. Civelli, and M. O. Goerbig, Magnetic-field-induced relativistic properties in type-i and type-ii weyl semimetals, *Phys. Rev. Lett.* **117**, 086402 (2016).
- [66] M. Udagawa and E. J. Bergholtz, Field-selective anomaly and chiral mode reversal in type-ii weyl materials, *Phys. Rev. Lett.* **117**, 086401 (2016).
- [67] P. Li, Y. Wen, X. He, Q. Zhang, C. Xia, Z.-M. Yu, S. A. Yang, Z. Zhu, H. N. Alshareef, and X.-X. Zhang, Evidence for topological type-II Weyl semimetal WTe₂, *Nature Communications* **8**, 2150 (2017).
- [68] L. Wang, I. Gutiérrez-Lezama, C. Barreteau, N. Ubrig, E. Giannini, and A. F. Morpurgo, Tuning magnetotransport in a compensated semimetal at the atomic scale, *Nature Communications* **6**, 8892 (2015).
- [69] A. C. Potter, I. Kimchi, and A. Vishwanath, Quantum oscillations from surface fermi arcs in weyl and dirac semimetals, *Nature Communications* **5**, 5161 (2014).
- [70] W. Tao, Z. J. Tong, A. Das, D.-Q. Ho, Y. Sato, M. Haze, J. Jia, Y. Que, F. Bussolotti, K. E. J. Goh, B. Wang, H. Lin, A. Bansil, S. Mukherjee, Y. Hasegawa, and B. Weber, Multiband superconductivity in strongly hybridized 1T-WTe₂/NbSe₂ heterostructures, *Phys. Rev. B* **105**, 094512 (2022).
- [71] Q. Li, C. He, Y. Wang, E. Liu, M. Wang, Y. Wang, J. Zeng, Z. Ma, T. Cao, C. Yi, N. Wang, K. Watanabe, T. Taniguchi, L. Shao, Y. Shi, X. Chen, S.-J. Liang, Q.-H. Wang, and F. Miao, Proximity-induced superconductivity with subgap anomaly in type II Weyl semi-metal WTe₂, *Nano Letters* **18**, 7962 (2018).
- [72] S. Shi, S. Liang, Z. Zhu, K. Cai, S. D. Pollard, Y. Wang, J. Wang, Q. Wang, P. He, J. Yu, G. Eda, G. Liang, and H. Yang, All-electric magnetization switching and Dzyaloshinskii-Moriya interaction in WTe₂/ferromagnet heterostructures, *Nature Nanotechnology* **14**, 945 (2019).
- [73] Y.-B. Choi, Y. Xie, C.-Z. Chen, J. Park, S.-B. Song, J. Yoon, B. J. Kim, T. Taniguchi, K. Watanabe, J. Kim, K. C. Fong, M. N. Ali, K. T. Law, and G.-H. Lee, Evidence of higher-order topology in multilayer WTe₂ from Josephson coupling through anisotropic hinge states, *Nature Materials* **19**, 974 (2020).
- [74] C.-Z. Chen, J. J. He, M. N. Ali, G.-H. Lee, K. C. Fong, and K. T. Law, Asymmetric Josephson effect in inversion symmetry breaking topological materials, *Phys. Rev. B* **98**, 075430 (2018).
- [75] Z. Fei, W. Zhao, T. A. Palomaki, B. Sun, M. K. Miller, Z. Zhao, J. Yan, X. Xu, and D. H. Cobden, Ferroelectric switching of a two-dimensional metal, *Nature* **560**, 336 (2018).
- [76] P. Sharma, F.-X. Xiang, D.-F. Shao, D. Zhang, E. Y. Tsybal, A. R. Hamilton, and J. Seidel, A room-temperature ferroelectric semimetal, *Science Advances* **5**, eaax5080 (2019).
- [77] S. Bhowal and N. A. Spaldin, Polar metals: Principles and prospects, *Annual Review of Materials Research* **53**, 53 (2023).
- [78] Y.-H. Song, Z.-Y. Jia, D. Zhang, X.-Y. Zhu, Z.-Q. Shi, H. Wang, L. Zhu, Q.-Q. Yuan, H. Zhang, D.-Y. Xing, and S.-C. Li, Observation of coulomb gap in the quan-

- tum spin Hall candidate single-layer 1T'-WTe₂, [Nature Communications](#) **9**, 4071 (2018).
- [79] Q. Gu, J. P. Carroll, S. Wang, S. Ran, C. Broyles, H. Siddiquee, N. P. Butch, S. R. Saha, J. Paglione, J. C. S. Davis, and X. Liu, Detection of a pair density wave state in UTe₂, [Nature](#) **618**, 921 (2023).
- [80] A. Aishwarya, J. May-Mann, A. Raghavan, L. Nie, M. Romanelli, S. Ran, S. R. Saha, J. Paglione, N. P. Butch, E. Fradkin, and V. Madhavan, Magnetic-field-sensitive charge density waves in the superconductor UTe₂, [Nature](#) **618**, 928 (2023).
- [81] S. K. Lewin, C. E. Frank, S. Ran, J. Paglione, and N. P. Butch, A review of UTe₂ at high magnetic fields, [Reports on Progress in Physics](#) **86**, 114501 (2023).
- [82] D. Aoki, J.-P. Brison, J. Flouquet, K. Ishida, G. Knebel, Y. Tokunaga, and Y. Yanase, Unconventional superconductivity in UTe₂, [Journal of Physics: Condensed Matter](#) **34**, 243002 (2022).

SUPPLEMENTARY INFORMATION

1. DEFECTS AND SURFACE OF WTe_2

WTe_2 belongs to the transition metal dichalcogenides. The crystalline structure of these materials is usually layered. In each layer, the transition metal is sandwiched between two chalcogen layers (either S, Se or Te). Each Te-W-Te layer is separated by weak van der Waals interactions along the c -axis. Within each layer, there are strong covalent bonds. In this material, the W atoms form zigzag chains along the a axis, as can be seen in the atomic structure shown in Fig. 1(c) of the main text. In topography images, we can see the Te atoms also forming chains along this direction. In the inset of Fig. 1(c) of the main text, we provide the atomic structure superposed to a high resolution topographic image. These features are also shown in Fig. S1, but in a field of view showing a few defects. We can clearly identify the Te rows and interstitials as well as vacancies. These are the two types of defects that we can identify on the surface of this material. We find either small point vacancies, indicated with a white arrow in Fig. S1(a) or bump-like features that we refer to as interstitials, indicated by a black arrow in Fig. S1(a).

To better understand the features found in the topography at defects, we performed first-principles calculations based on density functional theory (DFT) as implemented in the Quantum Espresso code. WTe_2 presents a primitive unit cell with 12 sites, showing an orthorhombic structure with the Space group Pnm21 and with lattice parameters of $a = 3.477 \text{ \AA}$, $b = 6.249 \text{ \AA}$ and $c = 14.0179 \text{ \AA}$. The 1T' phase is a distorted 1T phase where the Te atoms have distanced themselves from their hexagonal position around the W atom. The 1T' phase can be easily recognized and differentiated from the 1T phase by the presence of isolated zigzag chains of chalcogenide atoms that run vertically. We investigated: (i) the formation of a Te vacancy in the surface layer and (ii) the replacement of one Te atom by a W one providing an antisite defect. To model the experimental system, we constructed slabs of $4 \times 4 \times 2$ size containing four layers, ensuring a 13 \AA separation between neighbouring defects, which is enough to discard interactions between them.

We calculated the density of states at an energy of 100 meV and compared the result with topography experiments made at 100 mV (Fig. S1(a)). The high resolution topographies of a vacancy and an interstitial are shown in Fig. S1(b,c), respectively. Calculations are shown in Fig. S1(d,e). We note that the calculations nicely reproduce the elevated density of states along the Te chains, giving the characteristic row-like structure of STM images in WTe_2 . The row-like structure is broken at the defects. On Te vacancies (Fig. S1(b)) we find a clear black ‘‘hole’’ in a Te row, due to the missing Te atom. This ‘‘hole’’ is also found in the calculations (Fig. S1(d)). The chain like structure is compressed at the ‘‘hole’’ in experiments. This can be related to the features perpendic-

ular to the chains, which are observed in the calculations (Fig. S1(d)). On the other hand, calculations present (Fig. S1(e)) an increased density of states on interstitials (substitution of Te with W), with a highly asymmetric structure around the additional W atom, similar to a horseshoe. This structure is also observed in the experiment (Fig. S1(c)). Overall, the agreement between experiment and calculation is very good and, importantly, highlights that both W and Te derived orbitals contribute to the tunneling at atomic scale.

In the large scale STM topography (Fig. S1(a)), we see that these features are repeatedly observed over the image. We can estimate a density of defects of approximately $1.3 \times 10^{12} \text{ cm}^{-2}$. Using the lattice parameters $a = 3.5 \text{ \AA}$ and $b = 6.25 \text{ \AA}$, we can estimate that the electrons can move freely along ~ 336 unit cells, which gives a mean free path $\ell \sim 167.5 \text{ nm}$. Using the Drude model, we find a residual resistivity of $\rho = 1.95 \mu\Omega \cdot \text{cm}$ and mobility of $\mu = 4.26 \text{ m}^2/(\text{Vs})$. This agrees with previous reports and macroscopic characterization of our samples [19, 56].

In the STM topography (Fig. S1(a)) we also observe additional features at larger length scales around defects. These are related to the scattering pattern observed when making conductance maps at different bias voltages to obtain the QPI results discussed in Fig. 2 of the main text and further discussed in the following section.

2. QUASIPARTICLE INTERFERENCE SCATTERING

The relation between the measured local density of states and the momentum eigenstates $\Psi(\vec{r}_k)$ is given by

$$LDOS(E, \vec{r}) \propto \sum_{\vec{k}} |\Psi(\vec{r}_k)|^2 \delta(E - \epsilon(\vec{k})), \quad (1)$$

where $\epsilon(\vec{k})$ is the dispersion relation of the material. When the periodicity of the crystal is broken by the presence of impurities or defects on the surface, electrons are scattered, producing oscillations in the $LDOS$. These scattering processes are typically elastic. In this picture, scattering between states with \vec{k}_1 and \vec{k}_2 gives rise to a modulation with $\vec{q} = \vec{k}_1 - \vec{k}_2$ in the $LDOS$ that can be observed in the tunneling conductance with the STM. The scattering between an initial state, i , and a final state, f , is described by the Fermi golden rule,

$$\omega(i \rightarrow f) \propto \frac{2\pi}{\hbar} |V(\vec{q})|^2 N_i(E_i, \vec{k}_i) N_f(E_f, \vec{k}_f), \quad (2)$$

where $E_i = E_f$ for elastic scattering, $\vec{q} = \vec{k}_f - \vec{k}_i$ is the scattering vector, N_i and N_f the initial and final density of states, and $V(\vec{q})$ the scattering potential.

To get some insights from calculation, we first performed DFT calculation in the way described in the

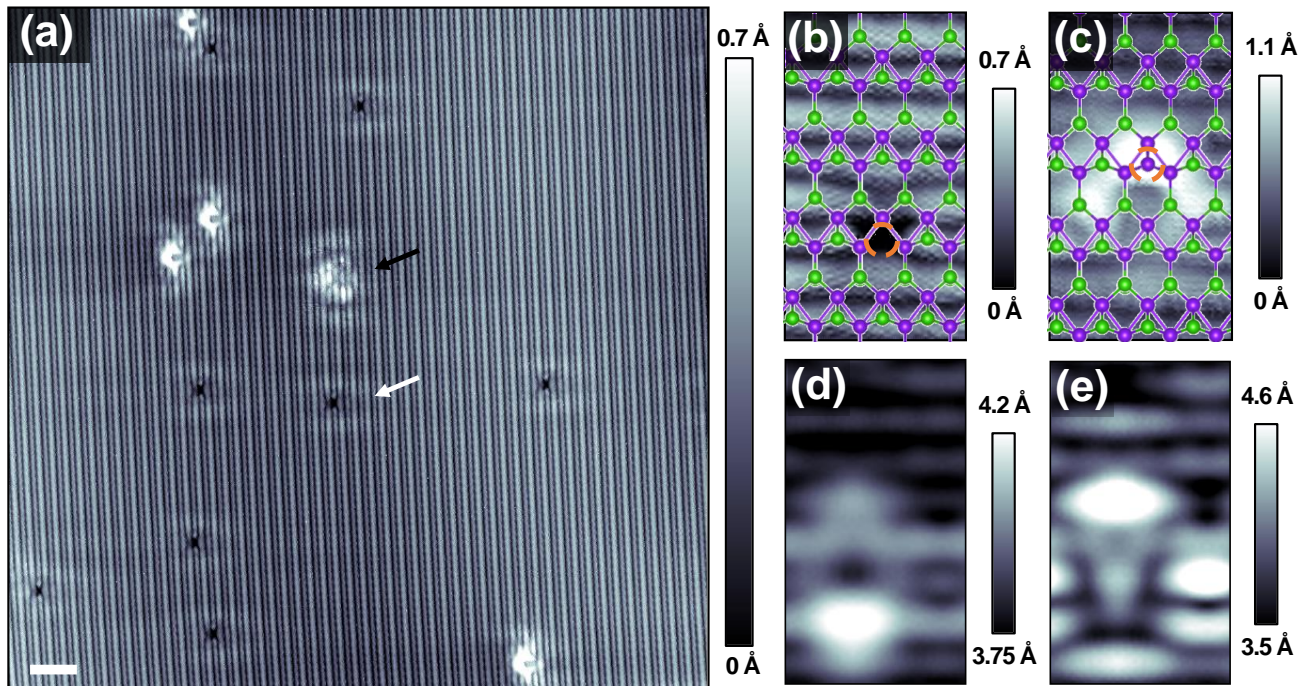


FIG. S1. (a) Large STM topographic image showing a region with different types of defects. White and black arrows mark vacancy-like defects and interstitials, respectively. Wavelike patterns can be seen coming due to scattering at the defects. Horizontal scale bar is 2 nm long. (b,c) Zoom into a vacancy (b) defect showing the lack of a surface Te atom and an interstitial (c) showing a substitution of Te by W. The surface pattern caused by this disruption is slightly asymmetric along the b-direction, as also shown in the calculations. (d,e) Calculated local density of states of a Te vacancy (d) and a substitution of W by Te (e). We again observe an asymmetry along the b-direction, also found in the calculations. Note that the maps (b-e) are rotated with respect to (a) so as to place the Te chains parallel to the x-axis. The atomic structure is superposed to the experiments in (b,c). Violet is for W and green for Te.

main text. After the first-principles calculation, we constructed the Wannier functions [83, 84] using the WANNIER90 software [85]. We did not perform the maximal localization procedure to prevent the mixture of the different spin components. We took the W-*d* and Te-*p* orbitals as the Wannier basis. Fermi surfaces and autocorrelation functions were calculated using the tight-binding model consisting of the Wannier functions. The autocorrelation function calculated in this study was defined as

$$I(E, \vec{q}) = \frac{1}{2} \sum_{\vec{k}, i, j} \sum_{l=0}^3 f_l(\vec{k}, \epsilon_i - E) f_l(\vec{k} + \vec{q}, \epsilon_j - E) \quad (3)$$

where $f_l(\vec{k}, \epsilon_i - E)$ is the Lorentzian function,

$$f_l(\vec{k}, \epsilon_i - E) = \frac{1}{\pi} \frac{\gamma}{(\epsilon_i - E)^2 + \gamma^2} \langle \sigma_l \rangle_i, \quad (4)$$

with the smearing width γ for the *i*-th Kohn-Sham energy ϵ_i and the expectation value of the Pauli matrix σ_l ($l = 0, 1, 2, 3$) for the corresponding eigenstate (see, e.g., Ref. [10], for a use of the spin-decomposed spectral density). To reduce computational cost, we constrained the summation on the $k_z = 0$ plane. We took $\gamma = 1$ meV and a 240×240 -mesh in the region of $|k_{x,y}| \leq 0.6\pi a^{-1}$.

The Fermi energy in all the calculated data was shifted by -45 meV so as to reproduce the experimental data.

We show in Fig. S2(a) the Fourier transform of the tunneling conductance maps, compared to calculations of the band structure (Fig. S2(b,c)). In Fig. S2(b) we show the constant energy contours of the band structure and in Fig. S2(c) their autocorrelation function. The latter is expected to reproduce some of the scattering features. Nevertheless, a full agreement is not to be expected, as the autocorrelation function just leads to a doubling in *k* space of the features of the constant energy contour, or a passage from \vec{k} to \vec{q} by geometrical construction, and does not account for k_z -summation nor the scattering potential $V(\vec{q})$.

We can now discuss the comparison between bulk band structure and experiment.

The dark and light violet and the magenta points refer to scattering between the two tiny W-derived pockets for large positive energies. Close to the light violet point at large wavevectors, there is a convex feature which is also seen in the autocorrelation function Fig. S2(c). This convex feature is also there at 50 meV, but is much weaker or absent below 50 meV. As for the magenta points, these lead to convex features in both experiment and calculations at 75 mV. The dark violet feature leads to a concave

feature in the calculations. In the experiments, there is also a concave feature, but at the same time the curves clearly show a convex feature which is not seen in the calculations, for example at 75 mV. As we show below, the convex feature might be due to the surface state, although calculations locate the surface state at a slightly larger k_x .

On the other hand, scattering from the hole Te-derived pockets provides the green points shown for bias voltages and energies below approximately 0 meV. We see that the dark green scattering is generally associated to a concave feature in the autocorrelation function which is also seen in the experiment, particularly at -25 mV. At the lowest bias voltages, the experiments show a tendency to form convex features, which is not clearly seen in the calculations. This might be to the surface state discussed below. The light green points show generally convex features in experiment, except at -75 mV, which are however more concave like in the calculations. This, again, might be due to the surface states discussed below.

3. SURFACE STATES AND QPI

For surface-state calculation, the semi-infinite-slab tight-binding model was used for calculating the surface spectra in a way described in the literature [86]. The energy smearing of 0.1 meV was applied as the imaginary part of the denominator of the Green's function. For calculating the autocorrelation functions for the surface, $f_i(k, \epsilon_i - E)$ in Eq. (3) was replaced with the calculated surface spectrum.

To address with more detail the behavior at surface states, we start by analyzing the scattering pattern at the voltage range where surface states are expected to show up. From calculations, this might occur around -50 meV and around +75 meV. In Fig. S3 we show results and calculations at these energies and bias voltages (a,b at -50 meV and c,d at +75 meV). We mark the surface states in the constant energy contours by arrows in Fig. S3(a,c). These surface states join the electron (W-derived) and the hole (Te-derived) pockets. The Weyl points are expected to occur above the Fermi level at a finite k_x and k_y , as described in Ref. [12].

We then isolate the surface states (bottom panels of Fig. S3(a,c)) and make the autocorrelation function of the resulting images (top panels of Fig. S3(b,d)). We compare this with the experiment (middle panels of Fig. S3(b,d)) and with the autocorrelation from the bulk band structure (bottom panels of Fig. S3(b,d)).

We note that Fermi arcs imply a concave X-like feature crossing exactly $q_x = q_y = 0$ in the scattering pattern, as shown in top panels of Fig. S3(b,d) and predicted in Ref. [87]. This feature is indeed found in the experiment (middle panels of Fig. S3(b,d)) but its extension along q_y is somewhat larger than in the autocorrelation function. The other features of surface states are also observed in the experiment. The convex feature associ-

ated to the light green point in Fig. S3(b) is clearly seen in the experiment (middle panel of Fig. S3(b)) and the surface calculations (top panel of Fig. S3(b)), but absent in the bulk calculations (bottom panel of Fig. S3(b)). Furthermore, the large convex feature at the light violet point in Fig. S3(d) is seen in experiment (middle panel of Fig. S3(d)) and surface calculations (top panel of Fig. S3(d)). There is a similar feature in the bulk calculations (bottom panel of Fig. S3(d)). However, there is a much stronger convex feature on the dark violet point (middle panel), which is absent in the bulk calculations (bottom panel of Fig. S3(d)). This feature might be associated to the well established convex feature observed in the surface calculations (top panel of Fig. S3(d)) at a larger wavevector.

Thus, although the precise separation between bulk and surface states remains difficult due to the multiplicity of scattering features, in all there is consistent evidence for the presence of surface states, further supported by Landau quantization as discussed below.

It is difficult to compare with angular resolved photoemission (ARPES) results which focus at higher energies and filled states [51]. But there is a general agreement. ARPES is mostly sensitive to the hole-like Te derived pockets and their structure well below the Fermi level. However, high resolution ARPES provides the same convex features in the hole pockets at small k_x that we observe here and shows in addition that these hole pockets move below the Fermi level when increasing temperature above 160 K [18, 19]. Furthermore, in ARPES, there is a band at larger k_x which crosses the Fermi level above approximately -50 meV which was first identified as stemming from an electron pocket [19], but could be related to the surface state discussed above, judging from the position in reciprocal space. These surface states are indeed measured in detail with ARPES in Ref. [18], where it is clearly shown that these are Fermi arcs. Although the features appear at a smaller wavevector, possibly because of slightly shifted band structure, the observed bulk and surface band structure are mostly compatible with what we observe, including the Fermi arcs identified in Ref. [18].

4. SPATIALLY AVERAGED TUNNELING CONDUCTANCE VS MAGNETIC FIELD

Fig. S4(a) shows DFT band structure calculations in the same range than the STM measurements, along the $\Gamma - X$ direction. Electron and hole bands are plotted in purple and green respectively. Electron bands have a predominant $W - 5d$ character, while the hole bands have $Te - 5p$ character. The resulting momentum integrated density of states of these bands as a function of energy is represented in black in Fig. S4(b). We compare the calculated density of states to the spatially averaged tunneling conductance at different magnetic fields (colored lines in Fig. S4(b)). We see that the shape of spatially averaged

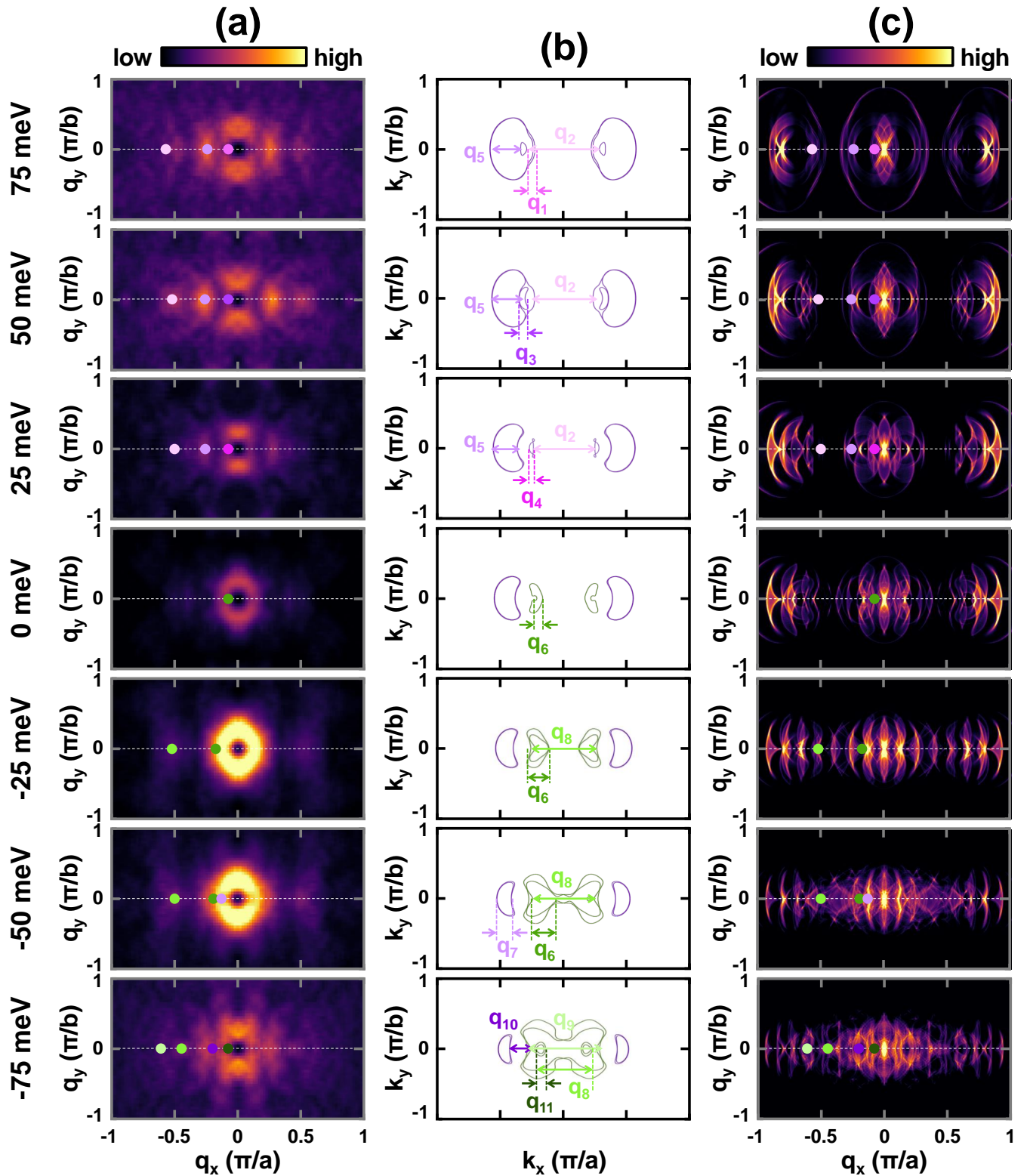


FIG. S2. (a) Fourier transforms of the conductance maps on a field of view containing defects (interstitials as well as vacancies, similar to Fig. S1(a)). The corresponding bias voltage is shown at the left of each panel. We show a few bias voltages, for clarity. The scattering intensity is shown by the color scale on the top. We indicate by colored points the scattering features that lead to the identify the scattering vectors q_1 to q_{11} shown in Fig. 2(b) of the main text for $k_y = 0$. (b) Calculated constant energy contours of the band structure. We show by colored arrows the scattering signal associated to the points in (a), with the same color code. (c) Autocorrelation of the calculated constant energy contours. Again, relevant features are shown as colored points.

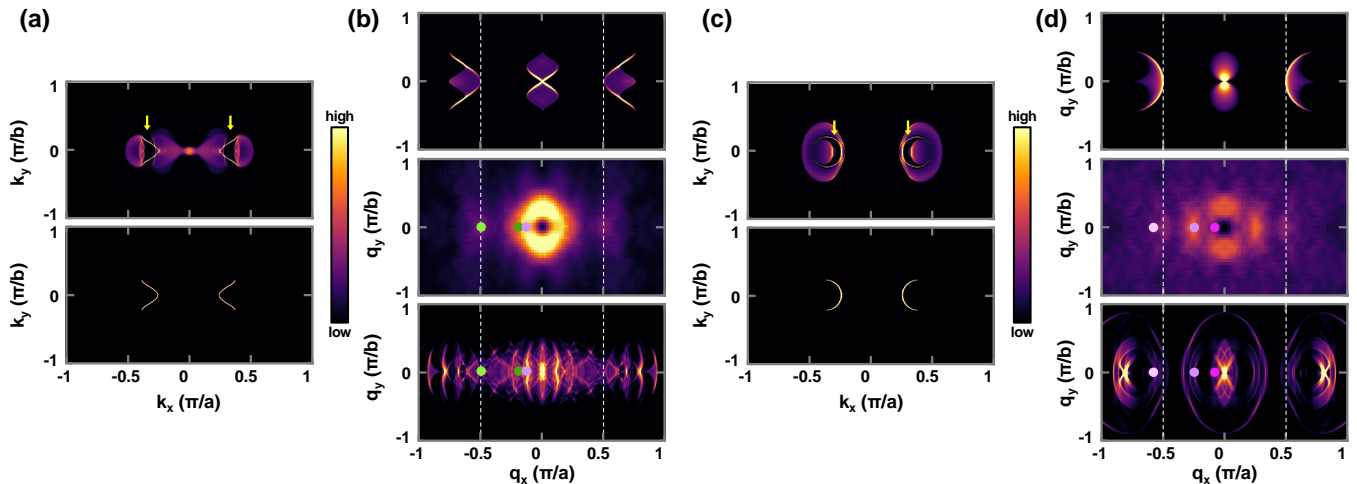


FIG. S3. (a) In the top panel we show the constant energy contour at -50 meV of the surface band structure of WTe_2 . We highlight by two yellow arrows the position of the surface state joining W-derived electron with Te-derived hole bands. The surface state is shown separately in the bottom panel. (b) In the top panel we show the autocorrelation function of the surface state. In the middle panel we show the experiment at -50 mV. In the bottom panel we show the autocorrelation function of the bulk band structure. In (c,d) we show the same plots, for the surface state at $+75$ meV.

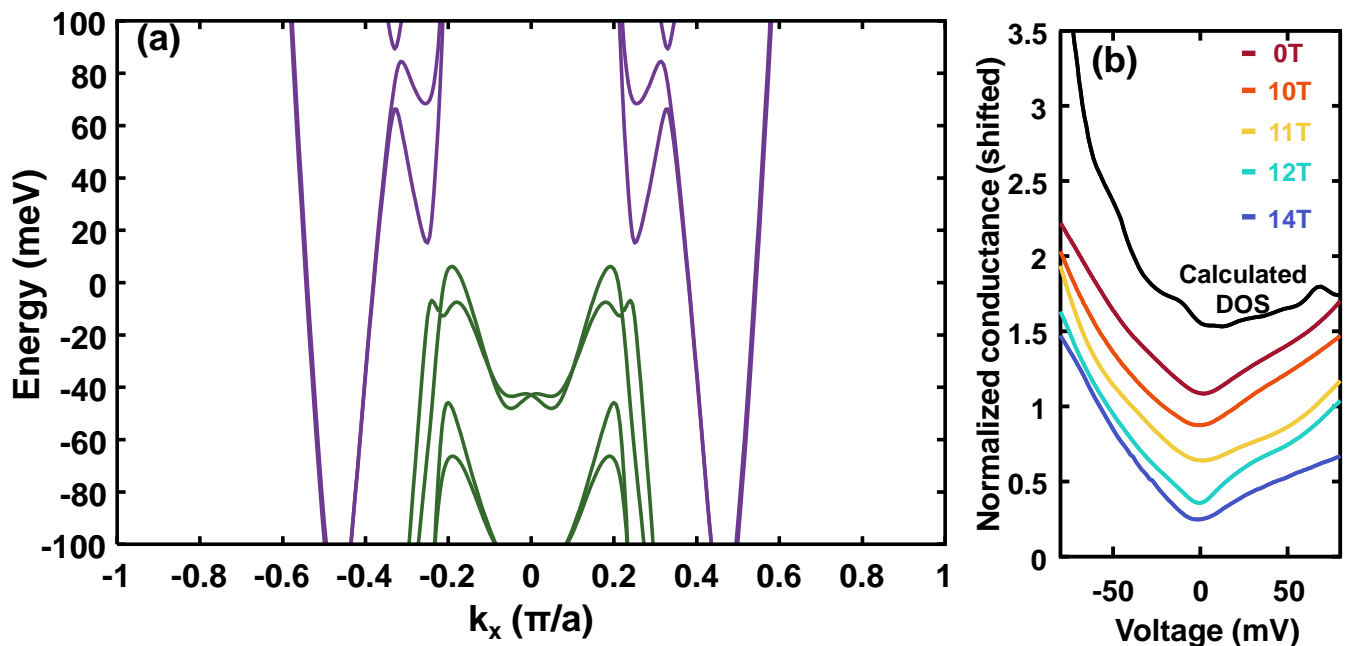


FIG. S4. (a) Calculated bulk band structure along the Γ ($k_x = 0$) to X ($k_x = 1$) direction inside the energy range explored in the experiment. Electron and hole bands are depicted in purple and green, respectively. Electron bands are derived from W 5d-orbitals and hole bands from Se 5p-orbitals. The calculations are shifted 45 meV downwards in energy to match our experimental results. (b) Spatially averaged normalized tunneling conductance versus bias voltage curves measured at magnetic fields ranging from 0 T to 14 T (colored lines). The normalized density of states obtained from the band structure in (a) is also plotted as a black line. Curves are shifted vertically for better visualization.

tunneling conductance curves vs bias voltage is similar to the shape of the calculated density of states vs energy.

It is of interest to ask how can one observe a huge increase, by more than six orders of magnitude, in the resistance when applying a magnetic field in WTe_2 , without any relevant magnetic field induced changes in the band structure. This shows that magnetoresistance is not caused by any change in the Fermi surface with magnetic field, but is rather associated to perfect electron-hole compensation, as proposed in Ref. [15, 31].

5. ATOMIC SCALE MAPS OF LANDAU QUANTIZED TUNNELING CONDUCTANCE

As we have discussed, our data show that Landau quantization is observed in WTe_2 with STM when taking tunneling conductance curves with atomic precision. We show in Fig. S5 the tunneling conductance as a function of the position along a line on top of Te atoms. We observe that the oscillations due to Landau levels shown in Fig. 3 of the main text change as a function of the position (Fig. S5(a)). We can obtain a similar map taking a spatially varying density of states $N_{local}(E, x) = \sum_n \left[E - E_0 - \sqrt{2e\hbar v_F^2 |n| B + A \cos(qx)} \right]^{-\frac{1}{2}}$. We use $A = 4.2$ mV, $v_F = 2.8 \times 10^5$ m/s and $q = 2\pi a$, where a is the unit cell parameter in the direction of the Te chains. Note that A is larger than $\hbar\omega_c/2$. Hence, the result is not a simple cosine wave, but an intricate set of maxima and minima, as shown in Fig. S5(b).

More information can be found if we take a closer look on the behavior under magnetic fields. Surface features are purely two-dimensional, and the Landau quantization should occur without any k_z dispersion and should thus be stronger. We can indeed find evidence of two surface states when looking at the amplitude of the Landau levels at different atomic positions. We can see in Figure S6 that the amplitude of the Landau oscillations for the curves taken between Te atoms (violet arrow), which corresponds to the position of the W atom, the conductance increases below -50 mV and above +75 mV. In Fig. S6(b) we show the conductance curves for four consecutive W atoms, and the grey shadow indicates the bias voltage range where the amplitude in the conductance oscillations increases. When looking at the conductance curves taken on top of the Te atoms (green arrow), the conductance increases below -50 mV. Figure S6(c) shows the conductance curves taken on top of four consecutive Te positions.

6. PROPERTIES OF DEFECTS

To further understand the role of defects, we carried out first principles calculations based on spin-polarized DFT in the plane wave formalism as implemented in the QuantumESPRESSO package [88]. We described the exchange-correlation energy by the generalized gradient approximation (GGA) using the Perdew–Burke–Ernzerhof (PBE) functional [89] and standard Ultra-soft (USPP) solid-state pseudopotentials extracted from the Materials Cloud Database. The electronic wave functions were expanded with well-converged kinetic energy cut-offs for the wave functions (charge density) of 50 (400) Ry. Van der Waals interactions between layers were considered by applying semiempirical Grimme-D3 corrections. We optimized atomic positions by using the Broyden–Fletcher–Goldfarb–Shanno (BFGS) algorithm until the forces on each atom were smaller than 10^{-5} Ry/au and the energy difference between two consecutive relaxation steps was less than 10^{-7} Ry. The Brillouin zone was sampled by a fine Γ -centered $3 \times 2 \times 1$ k-point Monkhorst-Pack [90]. To avoid unphysical interactions between images along the non-periodic direction, we added a vacuum of 18 Å along the z direction.

For the Te vacancy defect (Fig. S7(b)) we considered two different W sites, according to the W atom coordination. We found antiferromagnetic correlation between the two different W sites in the entire range of U, resulting in a global positive magnetic moment (Fig. S7(b)). From the spin-isosurface representation, we observed that there is a tendency for a two-fold arrangement (Fig. S7(c)), which is corroborated in the STM topography (Fig. S1(b)). For the W interstitial defect, there are three different W inequivalent sites, as a function of the W coordination (Fig. S7(d)). There one can observe that W atoms around the interstitial defect carry magnetic moments with ferromagnetic interactions between them and antiferromagnetically coupled with the interstitial W defect for the whole range of U (Fig. S7(e)). This results in a small magnetization. In all the defects produce pronounced changes in the band structure at the local level which could have some influence on the scattering potential $V(\vec{q})$, favoring certain directions in scattering and helping to observe the shape of the band structure out of the a direction discussed above. Other than that, we expect that the specificities of the band structure at Te vacancies and W-Te substitutions have a small effect in the scattering results.

[83] N. Marzari and D. Vanderbilt, Maximally localized generalized wannier functions for composite energy bands, *Phys. Rev. B* **56**, 12847 (1997).

[84] I. Souza, N. Marzari, and D. Vanderbilt, Maximally local-

ized wannier functions for entangled energy bands, *Phys. Rev. B* **65**, 035109 (2001).

[85] G. Pizzi, V. Vitale, R. Arita, S. Blügel, F. Freimuth, G. Géranton, M. Gibertini, D. Gresch, C. Johnson,

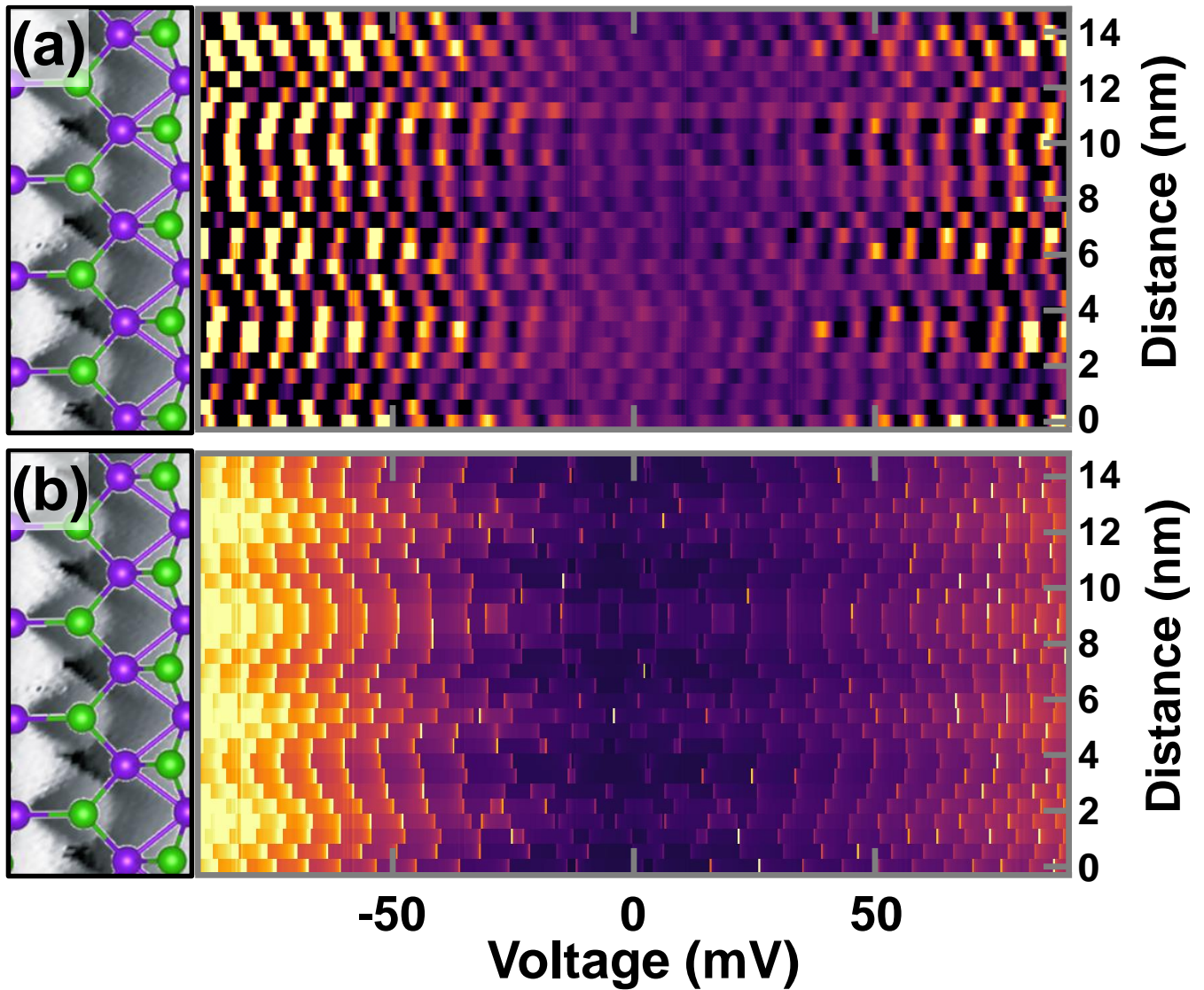


FIG. S5. (a) Tunneling conductance along a row following the a axis, taken at 14 T. In the left panel we show a topography of the surface, scaled to match the distance and atomic locations in the y -scale of the main panel. The map was obtained on top of a Te row. (b) Same as in (a), with a map obtained calculating the density of states as explained in the text, with parameters $A = 4.2$ mV and $q = 2\pi/a$. We use the same pixel size as in the experiment and the level separation measured for 14 T.

T. Koretsune, J. Ibañez-Azpiroz, H. Lee, J. Lihm, D. Marchand, A. Marrazzo, Y. Mokrousov, J. I. Mustafa, Y. Nohara, L. Paulatto, S. Poncé, T. Ponweiser, T. Ponweiser, J. Qiao, F. Thöle, S. Tsirkin, M. Wierzbowska, N. Marzari, D. Vanderbilt, I. Souza, A. A. Mostofi and J. R. Yates, Wannier90 as a community code: new features and applications, *J. Phys.: Condens. Matter* **32**, 165902 (2020).

- [86] M. P. L. Sancho, J. M. L. Sancho, and J. Rubio, Maximally localized wannier functions for entangled energy bands, *J. Phys. F: Met. Phys.* **15**, 851 (1985).
 [87] S. Kourtis, J. Li, Z. Wang, A. Yazdani, and B. A. Bernevig, Universal signatures of Fermi arcs in quasi-particle interference on the surface of Weyl semimetals, *Phys. Rev. B* **93**, 041109 (2016).
 [88] P. Giannozzi, S. Baroni, N. Bonini, M. Calandra, R. Car,

C. Cavazzoni, D. Ceresoli, G. L. Chiarotti, M. Cococcioni, I. Dabo, A. D. Corso, S. de Gironcoli, S. Fabris, G. Fratesi, R. Gebauer, U. Gerstmann, C. Gougoussis, A. Kokalj, M. Lazzeri, L. Martin-Samos, N. Marzari, F. Mauri, R. Mazzarello, S. Paolini, A. Pasquarello, L. Paulatto, C. Sbraccia, S. Scandolo, G. Sclauzero, A. P. Seitsonen, A. Smogunov, P. Umari, and R. M. Wentzcovitch, Quantum espresso: a modular and open-source software project for quantum simulations of materials, *Journal of Physics: Condensed Matter* **21**, 395502 (2009).

- [89] J. P. Perdew, K. Burke, and M. Ernzerhof, Generalized gradient approximation made simple, *Phys. Rev. Lett.* **77**, 3865 (1996).
 [90] H. J. Monkhorst and J. D. Pack, Special points for Brillouin-zone integrations, *Phys. Rev. B* **13**, 5188 (1976).

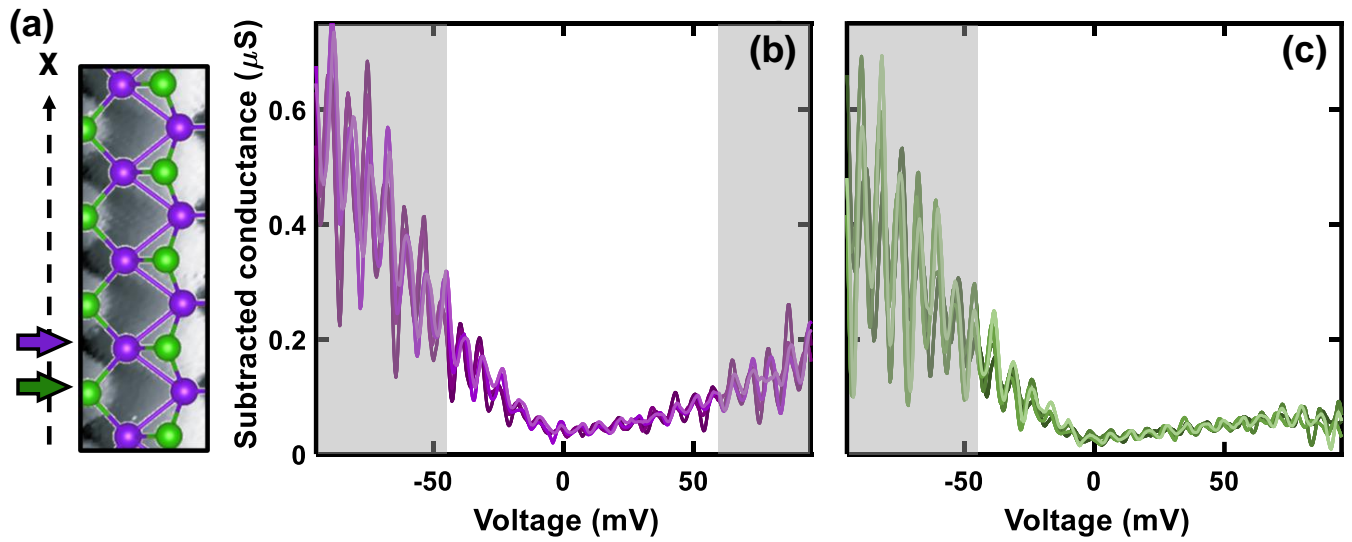


FIG. S6. (a) Zoom into the topography around a chain of Te atoms. Arrows provide schematically the atomic positions inside a unit cell where the curves in (b,c) were taken. (b) Tunneling conductance vs bias voltage obtained over four W atoms in four different unit cells. (c) Tunneling conductance vs bias voltage obtained over four Te atoms in four different unit cells. The grey background indicates the range above which two-dimensional surface states are expected within calculations (see text).

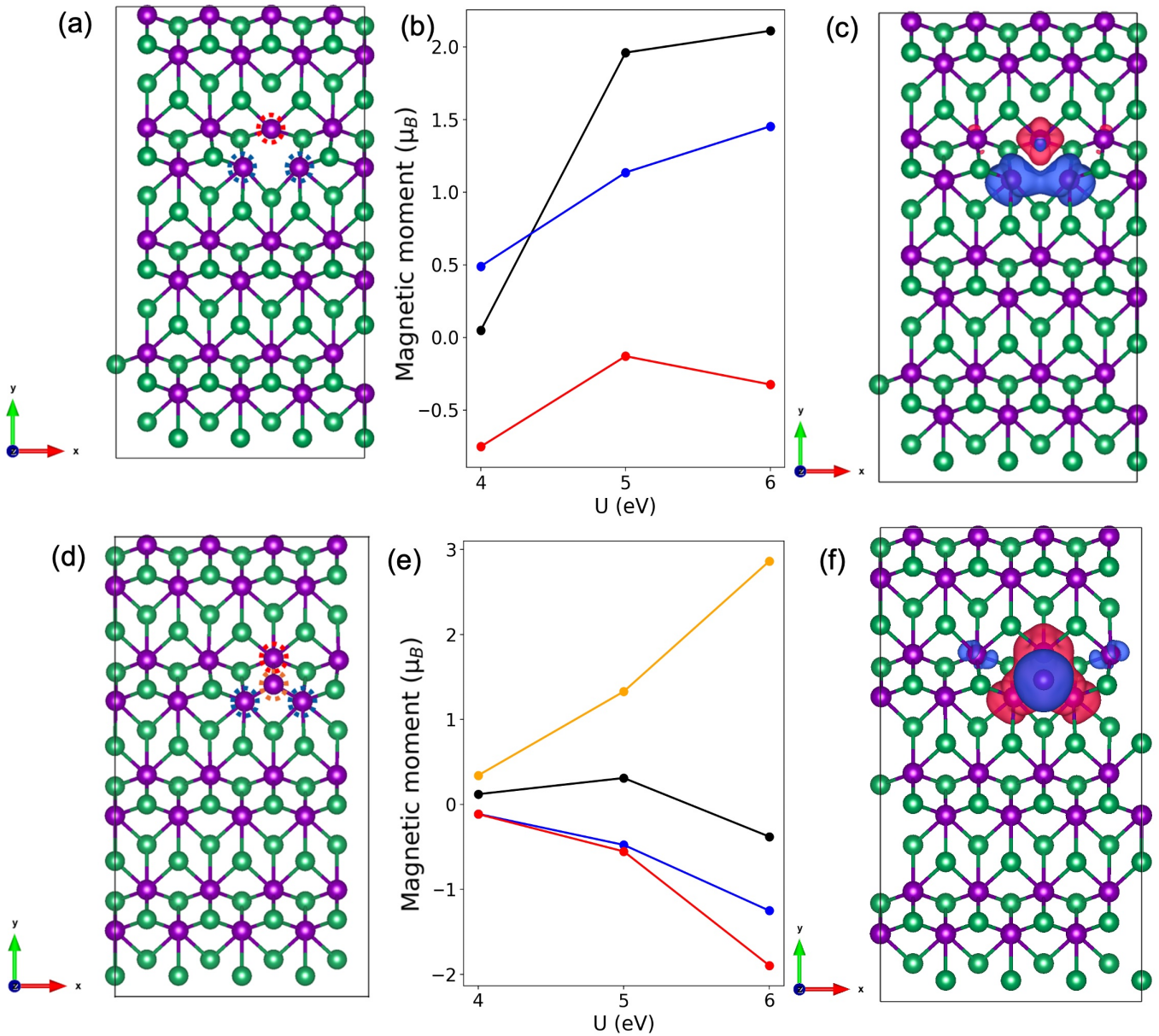


FIG. S7. (a) Surface atomic arrangement around a defect. We highlight the two types of W atoms around the interstitials, according to their bonding, with dashed circles. (b) Magnetic moment as a function of the Hubbard U parameter. We see that magnetic moments are essentially compensated, giving antiferromagnetic coupling, except for large U . (c) Spin isosurface, corresponding to a spin imbalance of 0.003 in red (spin down) and blue (spin up) and $U=5$ eV. Different atomic species are shown in colors, following the legend in (a,d).